# New capabilities in high-resolution neutron Larmor diffraction at ORNL

Li, Fankang; Feng, Hao; Parnell, Steven; Crow, Lowell; Matsuda, Masaaki; Ye, Feng; Kimura, Tsuyoshi; Fernandez-Baca, Jaime; Pynn, Roger; Thaler, Alexander N.

**DOI**
10.1107/S1600576718004211

**Publication date**
2018

**Published in**
Journal of Applied Crystallography

JOURNAL OF APPLIED CRYSTALLOGRAPHY

ISSN 1600-5767

# New capabilities in high-resolution neutron Larmor diffraction at ORNL[1]

Fankang Li,[a]* Hao Feng,[b] Alexander N. Thaler,[a] Steven R. Parnell,[c] Lowell Crow,[a] Masaaki Matsuda,[a] Feng Ye,[a] Tsuyoshi Kimura,[d] Jaime A. Fernandez-Baca[a] and Roger Pynn[a,b]

[a]Neutron Sciences Directorate, Oak Ridge National Laboratory, Oak Ridge, TN 37830, USA, [b]Center for Exploration of Energy and Matter, Indiana University, Bloomington, IN 47408, USA, [c]Faculty of Applied Sciences, Delft University of Technology, Mekelweg 15, Delft, JB 2629, The Netherlands, and [d]Department of Advanced Materials Science, University of Tokyo, Kashiwa, Chiba 277-8561, Japan. *Correspondence e-mail: fankangli@hotmail.com

Received 13 October 2017
Accepted 12 March 2018

Edited by D. Neumann, National Institute of Standards and Technology, Gaithersburg, USA

[1] This article will form part of a virtual special issue on advanced neutron scattering instrumentation, marking the 50th anniversary of the journal.

**Keywords:** Larmor diffraction; magnetic Wollaston prisms; neutron spin Larmor labelling; neutron precession; high-resolution diffraction.

Using superconducting magnetic Wollaston prisms, high-resolution neutron Larmor diffraction has been implemented at the High-Flux Isotope Reactor of Oak Ridge National Laboratory (ORNL), Tennesse, USA. This technique allows the inverse relationship between the achievable diffraction resolution and the usable neutron flux to be overcome. Instead of employing physically tilted radio-frequency spin flippers, the method uses magnetic Wollaston prisms which are electromagnetically tuned by changing the field configurations in the device. As implemented, this method can be used to measure lattice-spacing changes induced, for example, by thermal expansion or strain with a resolution of $\Delta d/d \simeq 10^{-6}$, and the splitting of sharp Bragg peaks with a resolution of $\Delta d/d = 3 \times 10^{-4}$. The resolution for discerning a change in the profile of a Bragg peak is $\Delta d/d < 10^{-5}$. This is a remarkable degree of precision for a neutron diffractometer as compact as the one used in this implementation. Higher precision could be obtained by implementing this technique in an instrument with a larger footprint. The availability of this technique will provide an alternative when standard neutron diffraction methods fail and will greatly benefit the scientific communities that require high-resolution diffraction measurements.

## 1. Introduction

By measuring the diffraction angle and applying Bragg's law, conventional diffraction techniques using X-ray and neutron scattering have shown their importance in determining the atomic and/or magnetic structure of materials. To achieve a lattice-spacing resolution better than $\Delta d/d \simeq 10^{-3}$ is extremely challenging for neutrons owing to the beam divergence and relatively low neutron flux. However, the neutron, a particle with a magnetic moment of $\mu_n = -1.93\ \mu_N$, with $\mu_N$ being the nuclear magneton, provides us with an alternative way of approaching the problem by using the Larmor precession of its spin in a magnetic field (Bloch, 1946; Mezei, 1972). This method is termed Larmor labelling, and it has been used to encode the change in neutron energy (Mezei, 1972) and trajectory (Rekveldt, 2011). For energy encoding, dubbed neutron spin–echo (Mezei, 1972), the small energy change experienced as a result of quasi-elastic neutron scattering can be encoded into a change in the Larmor phase by using two solenoids whose magnetic fields are parallel to the neutron trajectories before and after scattering. For trajectory encoding, such as spin–echo small-angle neutron scattering (Rekveldt, 1996; Pynn *et al.*, 2005; Parnell *et al.*, 2015) or Larmor diffraction (Rekveldt *et al.*, 2001; Keller *et al.*, 2002),

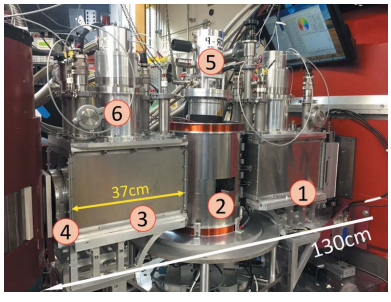

the change in the neutron trajectory due to interaction with the sample can also be labelled using the Larmor phase. By measuring the Larmor phase of the overall beam using a polarizing analyser, structural information about the sample can be recovered. Neutron Larmor diffraction, first introduced by Rekveldt *et al.* (2001), generates a Larmor phase that depends only on the scattering vector of the Bragg peak measured. Compared with high-resolution X-ray diffraction, neutron Larmor diffraction takes full advantage of the penetrating power of neutrons and allows us to measure samples containing light elements, like oxygen or carbon, as well as magnetic samples in some cases.

The neutron Larmor diffraction concept as introduced by Rekveldt *et al.* (2001) involves two rectangular regions of constant magnetic field, located before and after the sample, with their boundaries tilted to be parallel to the diffracting crystal planes in such a way that the total Larmor phase $\Phi$ produced by the setup is given by

$$\Phi = \frac{2m\omega_{\rm L}L}{\pi\hbar}\, d, \qquad (1)$$

where $m$ is the mass of the neutron, $\omega_{\rm L}$ is the Larmor frequency given by $\omega_{\rm L} = \gamma_{\rm n}B$ with $\gamma_{\rm n}$ the gyromagnetic ratio of the neutron and $B$ the magnetic field, $L$ is the size of the coil, $\hbar$ is the reduced Planck constant and $d$ is the lattice spacing (Rekveldt *et al.*, 2001). Thus, instead of directly measuring the change in the diffraction angle, this method allows the measurement of small changes in the lattice spacing through the change in the neutron Larmor phase $\Phi$, allowing poorly collimated neutron beams to be used and thereby overcoming the limitations imposed by the inverse relationship between the achievable resolution and the usable flux that apply to traditional diffraction measurements.

Even though the use of two rectangular DC electromagnets would be the most straightforward way of implementing Larmor diffraction, the tilt angle is highly constrained since the two electromagnets need to be long enough to reach a useful resolution range. Therefore, to date neutron Larmor diffraction has only been implemented using the neutron resonance spin–echo (NRSE) technique (Keller & Keimer, 2015) with thin radio-frequency (RF) neutron-resonant flippers rather than DC magnets, as shown in Fig. 1(*a*). The RF flippers work as external clocks (Gähler *et al.*, 1992), where the first bootstrap pair starts the clock of the incident neutrons and the second pair stops the clock and measures the time of neutron passage. Owing to energy exchange between the neutron spin and the RF flippers, the neutron polarization vectors will be modulated in the time domain in the zero-field regions between the two pairs of RF flippers. Effectively, the modulation in time is equivalent to that of precession in a static field with the same geometry as the zero-field regions defined by the two pairs of RF flippers (so-called zero-field precession). By using a so-called bootstrap mode (Golub & Gähler, 1987), the total Larmor phase given in equation (1) can be increased by a factor of four for the NRSE method compared with the DC method with the same dimensions and fields. This technique has been used with great success, for

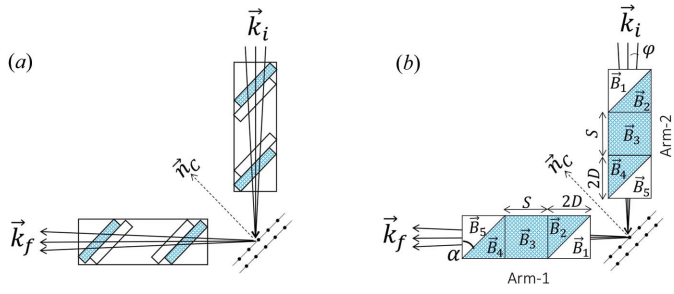


**Figure 1**
The Larmor diffraction setup using (*a*) RF spin flippers in bootstrap mode and (*b*) magnetic Wollaston prisms. For (*a*), the rectangles of different colours are the RF spin flippers with different field directions. They are enclosed inside a zero magnetic field chamber made of Mu metal with high magnetic permeability. The tuning is achieved when the field boundaries of the RF flippers are parallel to the crystal plane. For (*b*), each arm is composed of two superconducting magnetic Wollaston prisms with a rectangular field in between them. Regions of the same colour have the same magnetic field in terms of both magnitude and direction. All the field boundaries are provided by the Meissner effect of superconducting YBCO films (350 nm) coated on 0.5 mm sapphire plates (Li *et al.*, 2014). The tuning is achieved when the effective tilt angle of the magnetic field boundary [see equations (25) of the paper by Li & Pynn (2014)] matches the orientation of the crystal plane. $\alpha$ is the inclination angle of the hypotenuse film inside the Wollaston prism.

example to measure the structural and magnetic phase transitions in electron-doped iron pnictides (Lu *et al.*, 2016) and to study the formation of magnetostructural domains in yttrium barium copper oxides, YBCO (Náfrádi *et al.*, 2016).

Recently, we also demonstrated our approach to implementing Larmor diffraction using superconducting magnetic Wollaston prisms (Li *et al.*, 2017, 2014; Li, Parnell, Wang *et al.*, 2016), as shown in Fig. 1(*b*), and its principle has been explained and demonstrated (Li & Pynn, 2014; Li *et al.*, 2017). Basically, by using a series of magnetic field boundaries with or without inclinations, the method provides us with the possibility of tuning the effective field boundaries by picking different combinations of the fields. The inclined field boundary is provided by the triangular field regions of the magnetic Wollaston prisms, whose boundaries are defined by the Meissner effect of the superconducting YBCO films, as shown in Fig. 1(*b*). This eliminates the requirement to tilt the coils physically, which means a high effective tilt angle can be achieved. Though this approach is a DC method, the total Larmor phase does not take the simple form given in equation (1), owing to the electromagnetic tuning.

## 2. Larmor diffraction using magnetic Wollaston prisms

The details of tuning the effective tilt angle using magnetic Wollaston prisms have been discussed by Li *et al.* (2017) and Li & Pynn (2014) and the experimental tuning results are very close to the calculations. This provides us with confidence to tune the setup on the basis of the calculation results. Once the effective field boundary of the setup has been tuned with respect to the diffracting crystal planes, the accumulated total Larmor phase ($\Phi$) inside the device is only dependent on the $d$ spacing of the crystal and not, to lowest order, on the beam collimation or the crystal mosaic. With the polarization

analyser, only the projection of the polarization vector along the field direction of the analyser can be picked up, namely $\cos(\Phi)$. Therefore, for a crystal with a distribution of $d$ spacings whose mean value is $\overline{d}$, the induced Larmor phase variation is $\Phi = (d/\overline{d})\,\overline{\Phi}$ and the neutron polarization measured is the cosine Fourier transform of the distribution over all lattice spacings (Keller *et al.*, 2002),

$$P(\Phi) = \int f(d, \overline{d}, \sigma)\cos(\Phi)\,\delta(d). \tag{2}$$

Here, in the case of a simple Gaussian distribution of lattice spacings, $f(d, \overline{d}, \sigma)$ is the normalized distribution function of the lattice spacings, *i.e.*

$$f(d, \overline{d}, \sigma) = \frac{2}{\sigma}\left(\frac{\ln 2}{\pi}\right)^{1/2}\exp\left[-4\ln 2\left(\frac{d-\overline{d}}{\sigma}\right)^2\right], \tag{3}$$

where $\sigma$ is the full width at half-maximum (FWHM) of the distribution. In a more complicated case, as shown in Fig. 2($f$), if a Bragg peak is split into two peaks with lattice spacings of $d_1$ and $d_2$ and amplitudes $a_1$ and $a_2$, $f$ can be written as

$$f = a_1 f(d, d_1, \sigma_1) + a_2 f(d, d_2, \sigma_2) \quad \text{with} \quad d_1, d_2 = \overline{d} \mp \Delta d/2, \tag{4}$$

where $\overline{d}$ in this case is the average $d$ spacing of all Bragg peaks measured, *i.e.* $\overline{d} = (d_1 + d_2)/2$. Its cosine Fourier transform is given as

$$P(\Phi) = \Big[G(a_1, \sigma_1)^2 + G(a_2, \sigma_2)^2 + 2G(a_1, \sigma_1)G(a_2, \sigma_2)\cos\big(\Phi\Delta d/\overline{d}\big)\Big]^{1/2}, \tag{5}$$

where

$$G(a, \sigma) = a\exp\left(\frac{-\sigma^2\Phi^2}{16\ln 2}\right). \tag{6}$$

The measured trend of polarization $P(\Phi)$ is only dependent on the distribution of the $d$ spacings $\Delta d/d$ rather than on the mean value of the lattice spacing. For this reason, the following discussion will focus on the distribution of lattice spacings. Fig. 2 shows examples of some potential results of Larmor diffraction experiments (top) and the corresponding distributions of the lattice spacings (bottom). Clearly, the measured polarization follows the general expectations for Fourier transformation. For a perfect crystal with a single-valued lattice spacing, the amplitude of the Larmor phase oscillations is constant. For a crystal with some broadening in $d$ spacing, the measured polarization would damp monotonically towards a high neutron Larmor phase. For a Bragg peak splitting, for example $d_1$ and $d_2$, each lattice spacing will correspond to an oscillating polarization with a certain frequency when scanning the Larmor phase. Therefore, these two different frequencies will beat with each other, achieving a maximum amplitude of the polarization oscillations when the relative phase difference between the polarization signals for the two Bragg peaks equals $2N\pi$. To be specific, the beating can be reflected by the oscillation caused by the $\cos(\Delta d/\overline{d})\Phi$ term in equation (5), as shown in Fig. 2($c$). When the phase between the two different frequencies is $(2N + 1)\pi$, they are completely out of phase and a minimum in the polarization will be obtained. For a two-peak splitting such as that in Fig. 2($f$), the relative splitting of the $d$ spacings, $\Delta d/d$, is given by $\pi/\Phi_{P=\mathrm{Min}}$, where $\Phi_{P=\mathrm{Min}}$ is the Larmor phase at the first minimum of the polarization (Fig. 2$c$). For example, if the first minimum of the $P(\Phi)$ curve is observed at $\Phi_{P=\mathrm{Min}} = 1000$ rad, the lattice splitting $\Delta d/d = \pi/1000$. So, to some extent, $\pi/\Phi_{P=\mathrm{Min}}$ gives a good estimate of the achievable resolution for measurements of the difference between two $d$ spacings that exist in the same sample. For measurements of the relative change in the $d$-spacing distribution profile (as a function of temperature, for example), the achievable resolution will be better ($<10^{-5}$) because we just need to focus on the point with the highest Larmor phase and see how it changes. As also shown in Fig. 2($c$), the population of the two lattice constants will affect the local amplitude of the oscillation and the broadening of each lattice constant will cause the overall damping of the polarization curve.

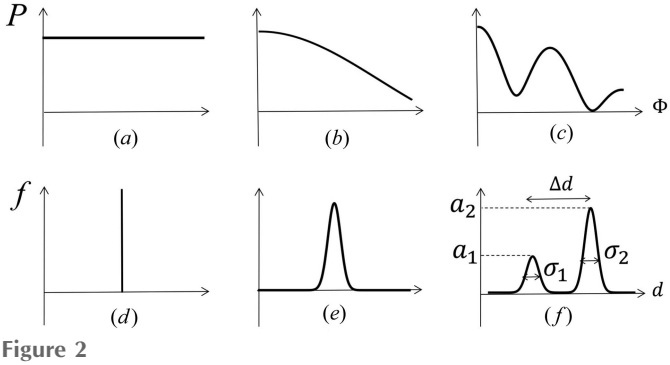


**Figure 2**
(Top row) Three typical results of Larmor diffraction measurements for demonstration, and (bottom row) their corresponding distributions of lattice spacings.

## 3. Lattice structural distortion measurements of $CuFeO_2$

The experimental setup for neutron Larmor diffraction with magnetic Wollaston prisms on the HB-1 polarized triple-axis

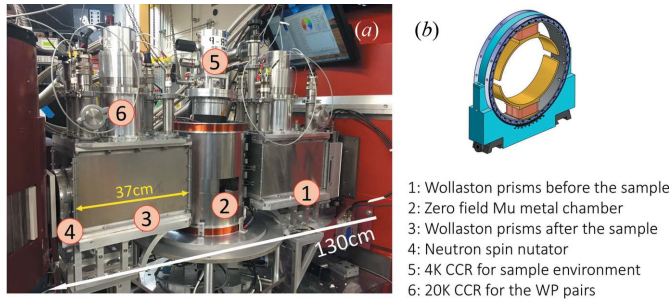


**Figure 3**
($a$) The experimental setup for Larmor diffraction on the HB-1 polarized triple-axis spectrometer (PTAX) at HFIR, shown in transmission geometry for better clarity. Neutrons travel from right to left. ($b$) A drawing of the nutator used in panel ($a$), which can create a magnetic field in any direction in the two-dimensional plane perpendicular to the beam. The space between the exit of the monochromator drum and the entrance of the analyser drum is ~130 cm and cannot be changed.

spectrometer (PTAX) at the High-Flux Isotope Reactor (HFIR) of Oak Ridge National Laboratory (ORNL), Tennesse, USA, is shown in Fig. 3, with the neutrons travelling from right to left straight through the sample. To minimize the magnetic stray field in the sample area, the two arms are surrounded by Mu metal plates on all four sides and these plates are connected to the Mu metal chamber for the sample (labelled 2). The stray field inside the Mu metal chamber can be minimized to <0.1 G using a series of compensation coils. The sample used for this measurement was $CuFeO_2$, which undergoes a first-order structural phase transition induced by the magnetic transition at 11 K and a second-order lower-symmetry lattice distortion at 14 K, seen using high-resolution synchrotron X-ray scattering performed on station 11-ID-C at the Advanced Photon Source, Argonne National Laboratory, Illinois, USA (Ye *et al.*, 2006). Since lattice expansion measurements on copper have already been demonstrated by Li *et al.* (2017), the following part will focus on lattice distortion measurements.

The neutron wavelength used for this measurement was 2.46 Å. Heusler (111) was used as monochromator and analyser. The horizontal collimator sequence was 48′–80′–60′–240′ and the contamination from higher-order beams was effectively eliminated using pyrolytic graphite filters.

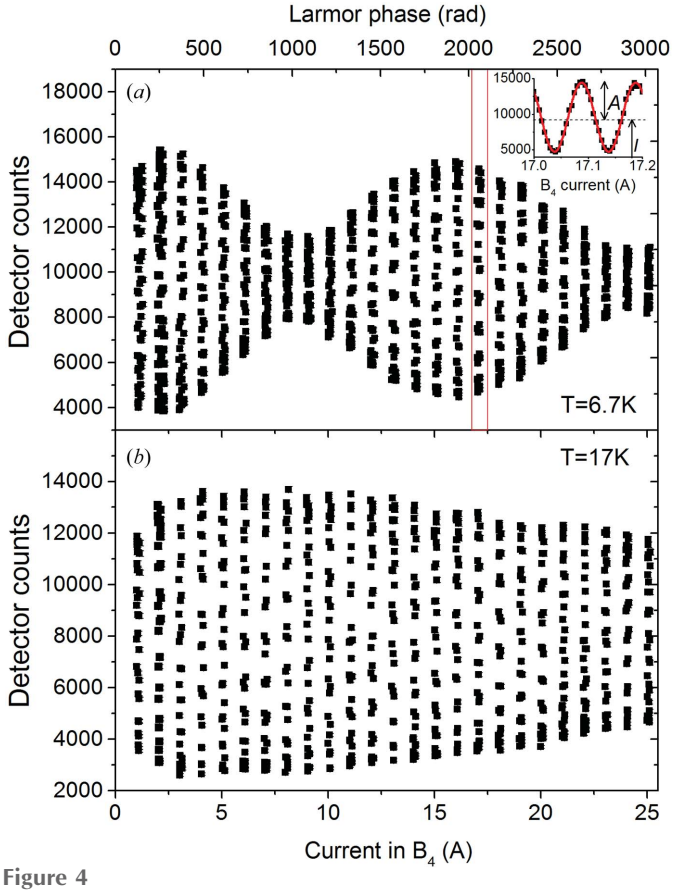


**Figure 4**
The fringes measured as a function of the current in $B_4$ (bottom axis) and the corresponding total Larmor phase (top axis). (*a*) $T$ = 6.7 K and (*b*) $T$ = 17 K. Each stripe in the plot corresponds to a fringe, shown in the inset plot in panel (*a*), which is measured by scanning the current in the device while maintaining the same effective tilt angle.

The measured Bragg peak of $CuFeO_2$ is (012) with $2\theta$ = 58.75°, so the tilt angle needed is $\beta$ = 60.6° [see equations (15) in the article by Li & Pynn (2014)], which means the magnetic field ratio needs to be set to $\gamma = B_4/B_5 = -4.87$ for the configuration shown in Fig. 1(*b*). For the NRSE method, the total Larmor phase is obtained by scanning the Larmor frequency $\omega_L$ in the RF flippers while keeping the physical field boundaries unchanged, and the polarization is then obtained by varying the distance between the RF flippers ($L$), as shown in Fig. 1(*a*). For our approach with Wollaston prisms, the total Larmor phase is varied by scanning the current inside the device while simultaneously maintaining the same effective tilt angle (*i.e.* $\gamma$ = constant). To minimize the measuring time, as shown in Fig. 4, the Larmor phase is only scanned at 25 current bands, which are the 25 stripes in the plot. For each current (stripe), the polarization ($P = A/I$) is obtained by varying the current in a small region, where $A$ and $I$ are the amplitude and shim intensity of the fringes shown in the inset of Fig. 4(*a*).

During the experiment, as shown in Fig. 4, the fringes as a function of the total Larmor phase are obtained for two different temperatures, 6.7 K in Fig. 4(*a*) and 17 K in Fig. 4(*b*). Clearly, the envelope of the fringes oscillates as a function of the Larmor phase at 6.7 K, while the oscillating feature disappears at 17 K, as reflected by the cosine term in equation (5). The scan of the total Larmor phase was repeated for

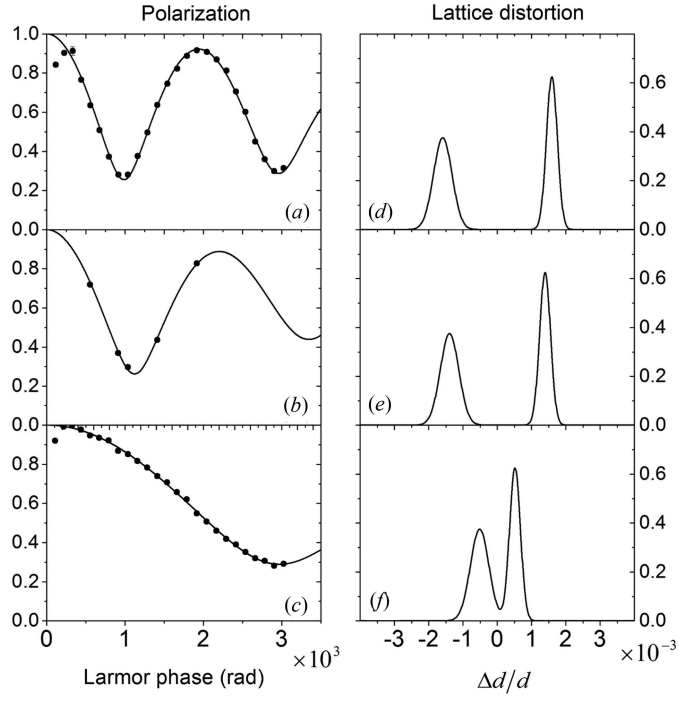


**Figure 5**
(Left) The normalized polarization as a function of the Larmor phase for (*a*) 6.7 K, (*b*) 9.9 K and (*c*) 12 K. (Right) The distribution of the lattice distortions $\Delta d/d$, with the lattice variation $\Delta d$ normalized to the mean value $d$ to fit the corresponding polarization on the left. For panel (*b*), the polarization efficiency was measured at only five different values of the Larmor phase to show how the data fit is sufficient with them. The populations and the FWHM of the split peaks are kept the same for the different temperatures.

various temperatures. The polarization efficiencies of all the fringes were extracted for all temperatures and normalized with respect to the polarization efficiency at 17 K. Some of the results are shown in Fig. 5. Here, results for three different temperatures with the polarization normalized are shown on the left and their corresponding distributions of the lattice constants fitted by equation (4) are given on the right-hand side. At 6.7 K, as shown in Fig. 5(*a*), where the structural distortion is significant, an oscillation can be observed in the polarization. As discussed earlier, this is due to the cosine term in equation (5), and the position of the first minimum gives us a good estimate of the absolute lattice distortion ($\Delta d/d = \pi/\Phi_{P=\mathrm{Min}}$). For Fig. 5(*b*), though only five points were obtained, the distribution of lattice constants can be obtained precisely by fitting once the minimum position is known. To obtain a high-resolution measurement of the peak splitting ($\Delta d/d$) in this case, the key is to maximize the achievable Larmor phase, for example by using longer-wavelength neutrons or by increasing the magnetic field intensity or the size of the device.

The peak splitting $\Delta d/d$ is plotted in Fig. 6 as a function of temperature, together with data obtained by X-ray diffraction which are shown as open circles. Clearly, the values measured by Larmor diffraction agree well with those obtained by X-ray diffraction below 12 K. The slight difference at 12 K is possibly due to the uncertainty in the temperature reading during the two experiments. This can be seen from the difference in the extrapolated critical temperatures for these two measurements, both of which should be 13.5 K.

## 4. Discussion

### 4.1. Collimation of the host triple-axis spectrometer

For this technique, the host triple-axis spectrometer (TAX) needs to be positioned to observe the Bragg peak of interest. Splitting of Bragg peaks due to structural distortion can be extremely hard to measure using a $2\theta$ scan of a TAX owing to beam divergence. By encoding the diffracted neutron trajectories into different Larmor phases, these split Bragg peaks are labelled with different Larmor phases, which causes the beating of the measured polarization as we observed above. A prerequisite condition of this technique is to capture all the diffracted neutrons from all the lattice distortions. For example, if the lattice distortion is large enough that some of the diffracted neutrons fall out of the detector or are cut off by the collimator after the sample, the setup is not performing a complete Fourier transform and we cannot get the correct answer. Therefore, Larmor diffraction is similar to other neutron Larmor labelling techniques (Parnell *et al.*, 2015; Li, Parnell, Bai *et al.*, 2016), in that all the scattered or diffracted neutrons need to be detected. From Bragg's law $\lambda = 2d\sin\theta$, to measure a lattice distortion of $\Delta d/d$ for a lattice spacing of $d$, the minimum collimation after the analyser is $\Delta\theta = \theta\tan(\theta)(\Delta d/d)$. For example, for $2\theta = 58.75^\circ$ and $\Delta d/d = 3 \times 10^{-3}$, the minimum collimation allowed for the outgoing neutrons is $\sim 0.05^\circ$, which is much smaller than the typical collimator used on the TAX. For incoming neutrons, the divergence of the neutron beam will cause Larmor phase aberration for the measured polarization and this will give an intrinsic resolution for the setup, as discussed by Rekveldt *et al.* (2014). So the incoming neutron beam needs to be well collimated.

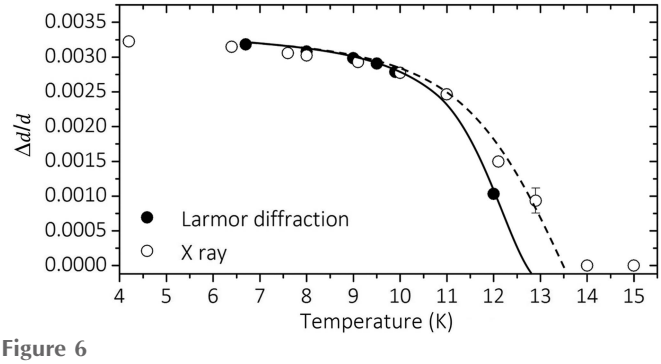


**Figure 6**
The measured $\Delta d/d$ as a function of temperature for $CuFeO_2$. The solid and open circles are the values obtained by Larmor diffraction and X-ray diffraction, respectively. Owing to the limited number of data points, the lines are included as a guide to the eye to show the critical temperature discrepancy between these two methods. The error bars for the Larmor diffraction measurements are smaller than the size of the points.

### 4.2. Optimization of the achievable Larmor phase

Fig. 1(*b*) shows only one of the configurations to operate the device for Larmor diffraction, to be specific, $B_1 = B_5$ and $B_2 = B_3 = B_4$. According to the work of Li & Pynn (2014), any

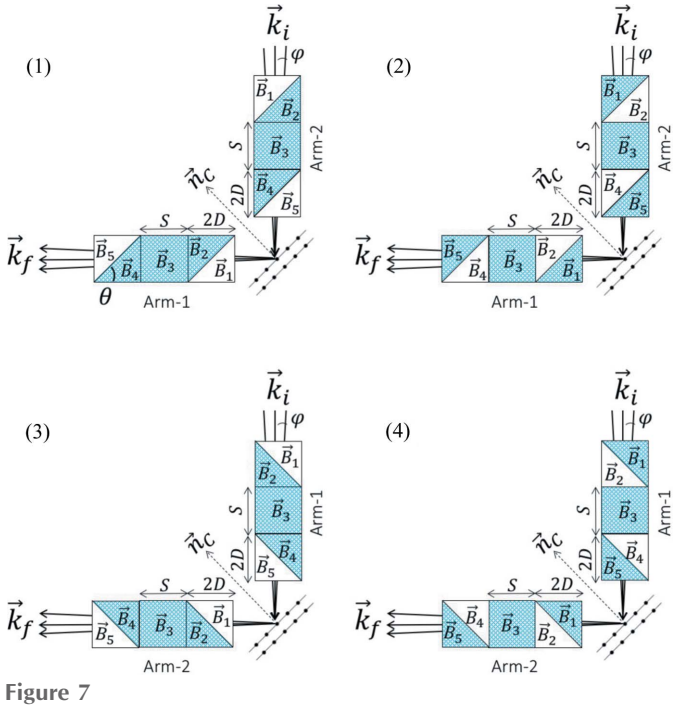


**Figure 7**
Schematic diagrams of the possible Larmor diffraction setups using the magnetic Wollaston prisms. Regions with the same colour have the same magnetic field intensity and direction. Arm-1 and Arm-2 denote the two different arms with different sense of hypotenuse. Compared with the configurations on the top row [(1) and (2)], the two arms are swapped in the bottom configurations [(3) and (4)].

**Table 1**
A chart for the possible field configurations in Fig. 7.

The configurations in (1) and (2) of Fig. 7 denote the cases of Arm-2 upstream and the configurations (3) and (4) have the two arms swapped. $\gamma_n$ is the gyromagnetic ratio of the neutron, $m$ is the neutron mass, $h$ is Planck's constant and $\lambda$ is the neutron wavelength.

| | Configuration | $\gamma = B_4/B_5$ | Total Larmor phase $\Phi$ ($\times\ \gamma_n m\lambda/h$) |
|---|---|---|---|
| (1) | $B_1 = B_5$, $B_2 = B_3 = B_4$ | $\dfrac{S+2D(1+\tan\beta)}{(S+2D)(1-\tan\beta)}$ | $2[(S+2D)\gamma + 2D]B_5$ |
| (2) | $B_2 = B_4$, $B_1 = B_3 = B_5$ | $\dfrac{(S+2D)(1+\tan\beta)}{S+2D(1-\tan\beta)}$ | $2[(S+2D) + 2D\gamma]B_5$ |
| (3) | $B_1 = B_5$, $B_2 = B_3 = B_4$ | $\dfrac{S+2D(1-\tan\beta)}{(S+2D)(1+\tan\beta)}$ | $2[(S+2D)\gamma + 2D]B_5$ |
| (4) | $B_2 = B_4$, $B_1 = B_3 = B_5$ | $\dfrac{(S+2D)(1-\tan\beta)}{S+2D(1+\tan\beta)}$ | $2[(S+2D) + 2D\gamma]B_5$ |

configuration that can keep $B_1 - B_2 + B_4 - B_5 = 0$ can be employed. Therefore, it could also be connected such that $B_2 = B_4$ and $B_1 = B_3 = B_5$. Since the sense of the hypotenuse films for the Wollaston prisms in these two arms are opposite to each other, these two arms can also be swapped with respect to the sample position. In principle, the rectangular field in between the two Wollaston prisms is not related to the field inside the Wollaston prisms but, to reduce the number of power supplies required and to simplify operation, it is connected in series to the other field regions. The possible Larmor diffraction setups using the Wollaston prisms are summarized in Fig. 7.

In Table 1, we list the configurations shown in Fig. 7, including the calculations of the ratio of $\gamma = B_4/B_5$ for a given tilt angle $\beta$ and the corresponding Larmor phase $\Phi$. As discussed earlier, the highest Larmor phase will determine the resolution of the setup. For each configuration, the highest achievable Larmor phase for each effective tilt angle has been calculated and plotted in Fig. 8. In these calculations, we have used certain parameters for our device, namely a maximum current of 50 A with a magnetic field of 35 G $A^{-1}$, a footprint of 37 cm for each arm and a neutron wavelength of 2.46 Å. Clearly, the highest Larmor phase of this technique is coupled with the effective tilt angles. Specifically, the overall Larmor phase for a high effective tilt angle is lower. For example, to achieve a tilt angle beyond 45° using the setup shown in Fig. 1(*b*), the field directions of $B_1$ and $B_5$ have to be the opposite of $B_2$, $B_3$ and $B_4$, which means the Larmor phase generated in $B_1$ and $B_5$ will be subtracted from that accumulated in $B_2$, $B_3$ and $B_4$. For an effective tilt angle lower than 45°, $B_1$ and $B_5$ need to be the same direction as $B_2$, $B_3$ and $B_4$, which will add additional Larmor phases. Equivalently, the effective tilt will lead to an effective size of the magnet, given as the coefficient of $B_5$ in Table 1. This is different from that of the NRSE technique, where the Larmor phase is a constant for all tilt angles, since the length of the flight path does not change when changing the tilt angles, as shown in Fig. 1(*a*). On the other hand, by introducing effective tilt using Wollaston prisms, the polarization and transmission efficiency of the setup are not affected when changing the effective tilt angle since no physical movement of the coils is required. From the calculations, we can see that configurations (1) and (4) are similar and always have the highest Larmor phase. With a maximum total Larmor phase of 12 000 rad, to observe at least one minimum in Fig. 2(*c*) for a measurement of Bragg peak splitting means a resolution of $\Delta d/d \simeq \pi/\Phi_{P=\mathrm{Min}} \simeq 3 \times 10^{-4}$. However, the resolution may be higher ($<10^{-5}$) for discerning a change in the profile of a Bragg peak as a function of an external parameter such as temperature. Currently, the achievable resolution is constrained by the available space on the beamline, as shown in Fig. 3, and the fact that the largest usable neutron wavelength is limited to 2.46 Å since the host TAX beamline is on a thermal neutron moderator.

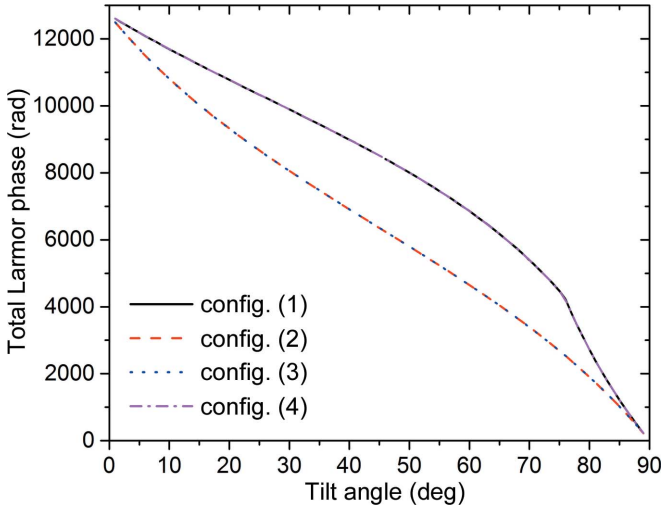


**Figure 8**
A map of the maximum accessible total Larmor phase for each configuration listed in Table 1. The maximum current allowed inside the device is 50 A and the magnetic field achieved is 35 G $A^{-1}$. The dimension used, as shown in Fig. 1, is $S = 2D = 10.5$ cm, and the wavelength used is 2.46 Å.

## 5. Conclusions

We have successfully implemented high-resolution neutron Larmor diffraction using superconducting magnetic Wollaston prisms on a polarized-neutron triple-axis spectrometer located at the HFIR at ORNL. Using this technique, we can measure the splitting of a sharp Bragg peak with a resolution of $\Delta d/d = 3 \times 10^{-4}$ and the resolution for discerning a change in the profile of a Bragg peak can be $\Delta d/d < 10^{-5}$. For lattice changes induced by thermal expansion or strain, a resolution better than that presented by Li & Pynn (2014) or Li *et al.* (2017) can be achieved. After 3–4 h of warming up the main power supply and employing another precise and stable power supply in parallel, a resolution of $\Delta d/d \simeq 10^{-6}$ has been achieved in measuring the thermal expansion. This is a remarkable degree of precision for a neutron diffraction setup as compact as the one used in this implementation. Although an X-ray diffractometer can be configured to achieve a similar

resolution, the wavelength spread needs to be minimized using a double-bounce monochromator and the method is limited to some specific samples. The achievable resolution of this setup is equivalent to that of the TRISP instrument at the FRM II reactor in Germany (Keller & Keimer, 2015).

YBCO is a type II superconductor, which means magnetic flux can penetrate when the YBCO film experiences a large enough perpendicular magnetic field (Brandt, 1996). To achieve an even higher field, and thus resolution, a thicker YBCO film is required and its development is still under investigation.

The purpose of involving two Wollaston prisms in each arm is to introduce a combination of inclined and non-inclined magnetic field boundaries such that the effective field boundaries can be varied by picking the right combination of them. The current inclination angle ($\alpha$ in Fig. 1) is 45°. For a given space available, reducing this angle can shrink the size of the Wollaston prism along the beam direction and thus increase the size of the rectangular field region in between, which can also be used to generate a larger Larmor phase without increasing the size of the device.

## Acknowledgements

We would like to acknowledge the team members of the High-Flux Isotope Reactor at Oak Ridge, Gerald Brent Taylor, Harish Agrawal, Ron G. Maples, John Ray Stout, Ron Conaway, John William Carruth, Stephen Kulan and Gary A. Taufer, for their help with these experiments. We are also indebted to Thomas Keller for useful discussions and support.

## Funding information

This research was sponsored by the Laboratory Directed Research and Development Program of Oak Ridge National Laboratory, managed by UT-Battelle, LLC, for the US Department of Energy. This research used resources at the High-Flux Isotope Reactor, a DOE Office of Science User Facility operated by the Oak Ridge National Laboratory.

## References

Bloch, F. (1946). *Phys. Rev.* **70**, 460–474.
Brandt, E. H. (1996). *Phys. Rev. B*, **54**, 4246–4264.
Gähler, R., Golub, R. & Keller, T. (1992). *Physica B*, **180–181**, 899–902.
Golub, R. & Gähler, R. (1987). *Phys. Lett. A*, **123**, 43–48.
Keller, T. & Keimer, B. (2015). *J. Large-Scale Res. Facil.* **1**, A37.
Keller, T., Rekveldt, M. T. & Habicht, K. (2002). *Appl. Phys. A*, **74**, s127–s129.
Li, F., Feng, H., Thaler, A. N., Parnell, S. R., Hamilton, W. A., Crow, L., Yang, W., Jones, A. B., Bai, H., Matsuda, M., Baxter, D. V., Keller, T., Fernandez-Baca, J. A. & Pynn, R. (2017). *Sci. Rep.* **7**, 865.
Li, F., Parnell, S. R., Bai, H., Yang, W., Hamilton, W. A., Maranville, B. B., Ashkar, R., Baxter, D. V., Cremer, J. T. & Pynn, R. (2016). *J. Appl. Cryst.* **49**, 55–63.
Li, F., Parnell, S. R., Hamilton, W. A., Maranville, B. B., Wang, T., Semerad, R., Baxter, D. V., Cremer, J. T. & Pynn, R. (2014). *Rev. Sci. Instrum.* **85**, 053303.
Li, F., Parnell, S. R., Wang, T., Baxter, D. V. & Pynn, R. (2016). *J. Phys. Conf. Ser.* **711**, 012015.
Li, F. & Pynn, R. (2014). *J. Appl. Cryst.* **47**, 1849–1854.
Lu, X., Tseng, K.-F., Keller, T., Zhang, W., Hu, D., Song, Y., Man, H., Park, J. T., Luo, H., Li, S., Nevidomskyy, A. H. & Dai, P. (2016). *Phys. Rev. B*, **93**, 134519.
Mezei, F. (1972). *Z. Phys.* **255**, 146–160.
Náfrádi, B., Keller, T., Hardy, F., Meingast, C., Erb, A. & Keimer, B. (2016). *Phys. Rev. Lett.* **116**, 047001.
Parnell, S. R., Washington, A. L., Li, K., Yan, H., Stonaha, P., Li, F., Wang, T., Walsh, A., Chen, W. C., Parnell, A. J., Fairclough, J. P. A., Baxter, D. V., Snow, W. M. & Pynn, R. (2015). *Rev. Sci. Instrum.* **86**, 023902.
Pynn, R., Fitzsimmons, M. R., Fritzsche, H., Gierlings, M., Major, J. & Jason, A. (2005). *Rev. Sci. Instrum.* **76**, 053902.
Rekveldt, M. T. (1996). *Nucl. Instrum. Methods Phys. Res. B*, **114**, 366–370.
Rekveldt, T. (2011). *Physica B*, **406**, 2324–2332.
Rekveldt, M. T., Keller, T. & Golub, R. (2001). *Europhys. Lett.* **54**, 342–346.
Rekveldt, M. T., Plomp, J. & van Well, A. A. (2014). *J. Appl. Cryst.* **47**, 436–442.
Ye, F., Ren, Y., Huang, Q., Fernandez-Baca, J. A., Dai, P., Lynn, J. W. & Kimura, T. (2006). *Phys. Rev. B*, **73**, 220404.